Materials Science & Engineering A 704 (2017) 154–163

Contents lists available at ScienceDirect

Materials Science & Engineering A

journal homepage: www.elsevier.com/locate/msea

Spark plasma sintering and spark plasma upsetting of an Al-Zn-Mg-Cu alloy

Mehmet Masum Tünçay[a,b], José Alberto Muñiz-Lerma[a], Donald Paul Bishop[c], Mathieu Brochu[a,*]

[a] Department of Mining and Materials Engineering, McGill University, 3610 University Street, Montreal, QC, Canada H3A 0C5
[b] Department of Metallurgical and Materials Engineering, Marmara University, 34722 Goztepe, Istanbul, Turkey
[c] Department of Process Engineering and Applied Science, Dalhousie University, 1360 Barrington Street, Halifax, NS, Canada B3J 1Z1

ARTICLE INFO

Keywords:
Spark plasma sintering
Forging
Al alloys
Mechanical properties

ABSTRACT

Al-Zn-Mg-Cu alloy powder Alumix 431D was sintered at 400 °C by spark plasma sintering (SPS) and upset forging was applied to the sintered sample through SPS. Densities of 99.1 ± 0.3% and 99.8 ± 0.1% of theoretical were obtained for the sintered and forged samples, respectively. T6 temper was carried out on the samples and microstructure analysis and mechanical properties before and after heat treatment were evaluated. Microhardness of 173 ± 3 and 172 ± 3 HV were attained in the T6 temper of as-sintered and forged samples, respectively. The flexural strength and strain values were significantly improved after the forging process, which can be mainly attributed to the better particle bonding in addition to the occurrence of some recrystallization. Significant loss in the ductility was observed after the T6 temper.

1. Introduction

Powder metallurgy (P/M), which is the manufacturing of parts from powder material, offers high material utilization, production of near-net shaped parts, and reduction or elimination of the costs related with complex machining operations [1–3]. Al P/M alloys have a wide range of applications such as hand tools, office machinery and automotive. Nevertheless, the properties of the conventional press and sinter parts are frequently insufficient for many of the more demanding applications envisioned for the technology [3]. Alumix 431D alloy, is a commercial powder blend composed of a mixture of pure Al with a master alloy containing Al, Zn, Mg and Cu. This powder blend is chemically similar to AA7075, and it is used in the fabrication of products requiring low weight and high strength [4].

A technical challenge inherent to P/M processing of Al alloys is the native oxide film present on the powder particles. This tenacious oxide layer of Al is highly stable from a thermodynamic standpoint and will prevent sintering if left intact during the processing cycle [5]. Thus, it is necessary to break the oxide layer in order to form appropriate metallurgical bonding between powder particles. Successful sintering of high strength Al alloys such as Alumix 431D alloy, can be obtained by liquid phase sintering, which is capable of disrupting the stable oxide layer covering the Al particles [6]. However, this manifests heterogeneous shrinkage of the powder compacts which is disadvantageous in the context of near-*net*-shape processing [6].

Spark Plasma Sintering (SPS) is an axial pressure-assisted process that uses joule heating from the passage of a high DC pulsed current through a graphite die and powder [7]. Solid state transport mechanisms (bulk and grain boundary) are favored during the process [8]. SPS is considered as an important process due to the ability to clean particle surfaces [9]. This is accomplished by contributing to the rupture of the oxide layer at the surface of the pure aluminum powder, which has been demonstrated in previous studies [10–17]. However, it has been shown by Garbiec and Siwak [18] and Rudinsky et al. [19] that Alumix 431 powder sintered by SPS exhibits low ductility during tensile or bending tests due to the lack of bonding between particles. It has been suggested that the formation of the spinel layer arising from the reaction of Mg and the alumina layer would impose the requirement for a higher applied load to break the oxide layer [20]. Alternatively, forging of aluminum P/M products is known to close the residual porosity and disrupts the oxide film around the powder particles because of the high strains and strain rates involved [1]. This enhances the metallurgical bonding across the interfaces where the oxide layer is broken [1]. Upsetting is a type of forging where a workpiece is reduced in dimension between two parallel plates and reduction in initial height without extensive spreading and substantial flow along the tool surface occurs [21].

The purpose of this study is to investigate the effect of hydraulic press forging [22] through SPS upsetting on the mechanical properties of Alumix 431D compact which is sintered by SPS. Bulk mechanical properties were measured through three-point bending test and correlated with fracture surface analyses in order to assess the nature of particle bonding. In addition, electron backscattered diffraction (EBSD) was also utilized to analyze the nominal grain size and grain boundary

* Corresponding author.
E-mail address: mathieu.brochu@mcgill.ca (M. Brochu).

http://dx.doi.org/10.1016/j.msea.2017.08.015
Received 23 May 2017; Received in revised form 23 July 2017; Accepted 3 August 2017
Available online 04 August 2017

Table 1
Chemical composition (wt%) of the Alumix 431D powder utilized.

Al	Zn	Mg	Cu	Sn
Bal.	6.1	2.5	1.6	0.3

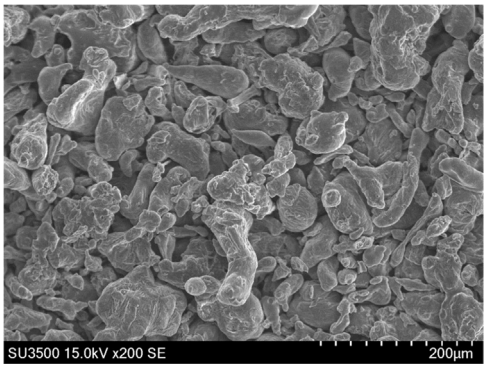

Fig. 1. SEM image of Alumix 431D powder.

mis-orientation angles after upset forging by SPS.

2. Experimental

Alumix 431D powder from ECKA granules with a chemical composition provided by the supplier's certificate of analysis, listed in Table 1, was used in the present study. A scanning electron microscopy (SEM) image of the starting powder is shown in Fig. 1. The morphology of the powder exhibits irregular shape as a result of production by air atomization.

A two-step process has been applied to the powder using SPS where the first step was the sintering of the powder and the second step was forging. A schematic of this process is presented in Fig. 2. Six cylindrical samples of 10 mm in height by 20 mm in diameter were spark plasma sintered using an SPS 10-3 apparatus from Thermal Technologies Inc., and using a 20 mm diameter Isocarb graphite I-85 die-punch set from Electrodes Inc. Sintering was performed at a temperature of 400 °C under 50 MPa of applied pressure and a 60 min holding time. The initial heating rate to reach 350 °C was 100 °C/min and a rate of 50 °C/min was applied subsequently up to 400 °C in order to avoid overshooting the target temperature. Temperature was measured using a C-type thermocouple placed in the bottom punch which had a hole drilled to 2 mm from the surface of the sample. The pressure was constant throughout the sintering cycle. Apart from sintering, a secondary forging process that imposed 32% compressive strain was applied to three sintered samples using the SPS apparatus. This represented the maximum amount of deformation that could be applied due to the limited length of the punch. This process was carried out by placing the 20 mm diameter sintered samples in a larger (25 mm diameter) Isocarb graphite I-85 die-punch set and heating them to 400 °C. All specimens were heated from ambient to 350 °C at rate of 100 °C/min and then at 50 °C/min from this point to the intended forging temperature of 400 °C. The samples were kept at 400 °C for a period of 4 min and then deformed at that temperature under a maximum pressure of 36 MPa, achieved by loading at 0.55 MPa/s which took 1 min to reach full pressure. The forged products were then cooled down to room temperature and removed from the SPS unit for analysis.

Bulk density was measured on sintered, forged and heat treated samples using the Archimedean method as described in ASTM standard B963-13 [23]. In order to heat treat the produced samples, differential scanning calorimetry (DSC) was first conducted with a NETZSCH STA 449F3 instrument to determine the initial melting temperature. For this purpose, 11 mg of the forged samples were heated up to 650 °C under flowing argon while using a heating rate of 10 °C/min. An initial melting event with a peak temperature of 475 °C, which corresponded to the melting of $MgZn_2$ phase [24], has been observed. Therefore, a solutionizing temperature of 450 °C was adopted. T6 temper was applied to both sintered and forged samples using 4 h solutionizing at 450 °C followed by artificial aging at 125 °C for 24 h after water quenching. The nomenclature and their descriptions for all of the samples are given in Table 2.

Sintered and forged samples (before and after heat treatment) were mounted, ground and polished using 320 and 400 grit papers, followed by 9 and 3 μm diamond suspensions with an end step of colloidal silica suspension on a Vibromet polisher. Microstructural analysis was performed with backscattered electron (BSE) imaging and energy dispersive spectroscopy (EDS) using a Hitachi SU3500 SEM. Electron backscattered diffraction (EBSD) was used to analyze the grain microstructure. X-ray diffraction (XRD) analysis was carried out using a Bruker D8 Discovery X-Ray Diffractometer (Cu-source radiation).

Mechanical properties were evaluated by microhardness and three-point bending tests. Microhardness was measured with a Clark Microhardness (CM-100AT) indenter using a load of 10 g. The reported hardness values represent an average of 10 indentations. Three-point bending tests (sample dimensions: 1.8 mm × 4.3 mm × 20 mm) were

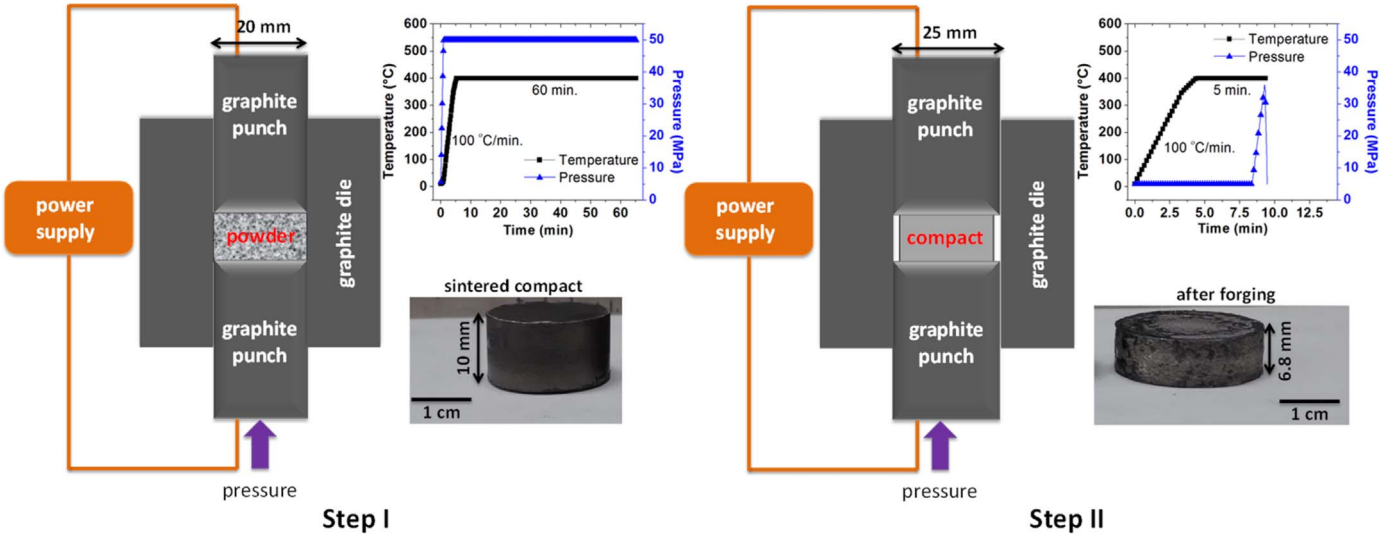

Fig. 2. Schematic of the two-step SPS process used in this study.

Table 2
Nomenclature and description of the samples processed.

Nomenclature	Description
T1	As-sintered (1 h at 400 °C under 50 MPa, furnace cool)
T6	Heat treatment of T1 sample (4 h at 450 °C, water quench, 24 h at 125 °C, air cool)
T1-forged	Upset forging of T1 sample (32% reduction in height at 400 °C after 4 min holding period, furnace cool)
T6-forged	Heat treatment of T1-forged sample (4 h at 450 °C, water quench, 24 h at 125 °C, air cool)

carried out using a Tinius Olsen load frame (model H25K-S) with a crosshead loading speed of 10 mm/min and a support span of 18.75 mm. The flexural stress and strain values were obtained using fundamental equations which can be found elsewhere [25]. Three tests were done on each sample type considered, i.e., T1, T1-forged, T6 and T6-forged. Fracture surface observations were performed with the aforementioned SEM.

3. Results and discussion

3.1. Spark plasma sintering

SPS of Alumix 431D powder was carried out and a density of 99.1 ± 0.3% theoretical density (TD) was obtained for the T1 condition considering 2.79 g/cm^3 as the full TD for the alloy [26]. The image analysis confirmed the value with a density of 99.3 ± 0.3%. A representative low magnification BSE micrograph taken after sintering is shown in Fig. 3. A low level of isolated rounded residual porosity remained after sintering as indicated by the annotated arrows. The microstructure was heterogeneous and was comprised of three distinct regions. High magnification BSE micrographs recorded from each of these regions are presented in Fig. 4. The first region (Fig. 4a) contained large amount of bright secondary phases that most likely correlated to remnants of the master alloy powders. The second and third regions (Fig. 4b and c) had progressively lower concentrations of secondary phases suggestive that they represented transformative states of the master alloy the alloying elements diffused away from it and into adjacent grains of pure aluminum. A similar behavior has been also reported by Rudinsky et al. [19] where it was ascribed to the insufficient diffusion distance of the alloying elements (Zn, Mg, Cu) to attain homogenization during SPS processing at 425 °C for 1 h.

XRD was then utilized in an effort to determine the principal phases present. The resultant spectrum (Fig. 5) indicated that α-Al and $MgZn_2$ were present consistent with the works of LaDelpha et al. [26], Rudinsky et al. [19], and Pieczonka et al. [27].

After sintering, a T6 heat treatment was applied to the T1 samples. The density of the T6 sample was 98.8 ± 0.2% TD. The density obtained by image analysis was 99.0 ± 0.2%, supporting the oil

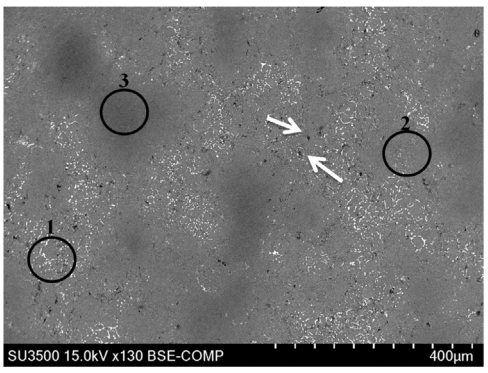

Fig. 3. Representative low magnification BSE micrograph of a T1 sample.

impregnation method. A representative BSE micrograph of a T6 tempered sample is shown in Fig. 6. It was observed from this microstructure that a considerable fraction of the secondary phases originally present in the as-sintered sample were now dissolved. However, in some isolated regions that contained the secondary phases were still present (for example, region 1 in Fig. 6).

High magnification BSE micrographs of the T6 sample are presented in Fig. 7 which corresponded to the three regions depicted in Fig. 6. It can be seen from Fig. 7a in comparison with Fig. 4a that the secondary phases were partially dissolved but some coarse precipitates remained in the microstructure. When compared to Fig. 4b, the microstructure in Fig. 7b was more homogenous. Finally, a homogenous microstructure was ultimately observed in Fig. 7c. These observations were substantiated via XRD as the spectrum recorded from the T6 sample (Fig. 5). In this sense, the intensity of all peaks ascribed to $MgZn_2$ had decreased appreciably but the phase remained readily detectable thereby supporting the notion of partial dissolution [28].

3.2. Spark plasma upsetting

In the next phase of research, upset forging within the SPS system was applied to the sintered samples. The final density of the forged products measured by oil impregnation and image analysis were 99.8 ± 0.1% TD. A representative low magnification BSE micrograph obtained from a T1-forged sample is depicted in Fig. 8. The level of remaining porosity in this condition was evidently decreased due to the forging treatment. However, as in the as-sintered samples, a heterogeneous microstructure consisting of the aforementioned three regions persisted. According to the XRD spectrum presented in Fig. 5, the $MgZn_2$ phase remained present in the T1-forged sample.

High magnification BSE micrographs of the three regions identified in Fig. 8 are presented in Fig. 9. The microstructure in region 1 consisted of large precipitates and when compared to region 1 of the as-sintered sample (Fig. 4a), coarsening of the precipitates was noted. Considering the fact that the forged samples were heated to 400 °C, this precipitate growth should be due to Ostwald ripening [29]. A similar behavior has been reported for hot deformed AA7050 alloy [30]. Additionally, Deschamps et al. [31] explained that the warm deformation accelerates the coarsening of the precipitates due to the formation of additional vacancies as a result of the plastic flow, which thereby enhances the kinetics of diffusion. Furthermore, it has been reported by Huo et al. [32] that $MgZn_2$ precipitates show a linear coarsening behavior with increasing warm rolling reduction of AA7075, which has likewise been attributed to the accelerated coarsening kinetics due to the plastic strain.

EBSD analysis of the T1-forged sample has been carried out and the map is shown in Fig. 10a. An orientation imaging microscopy (OIM) reconstruction was performed and the result is shown in Fig. 10b. The mis-orientation angles of the grain boundaries can be distinguished by colors: blue lines for 2–5°; red lines for 5–15°; thin black lines for 15–30°; bold black lines for > 30°. Boundaries having mis-orientation angles greater than 15° are called high angle boundaries and those smaller than 15° are called low angle boundaries [33]. The grain structure in Fig. 10b contained sub-grain boundaries which are represented by blue and red colors. Observation of these features in the hot deformed crystalline materials was an indication of dynamic recovery (DRV) [34] which is known to occur during hot deformation of Al alloys [33,35–37]. Additionally, there are some regions in Fig. 10b (i.e. circles 1, 2, and 3) where small equiaxed grains with high angle boundaries prevailed thereby indicating that recrystallization had occurred as well [36]. It has been described by McQueen [38] that Al-Mg alloys with a Mg content greater than 1% shows static recrystallization (SRX) after deformation during the cooling period. Rupp et al. [36] have demonstrated that SRX occurred in a Al-4.5% wt. Mg alloy even in the as quenched condition, which was deformed at 400 °C and 500 °C with 0.5 strain. It has been explained by McQueen [39] and Zaidi and

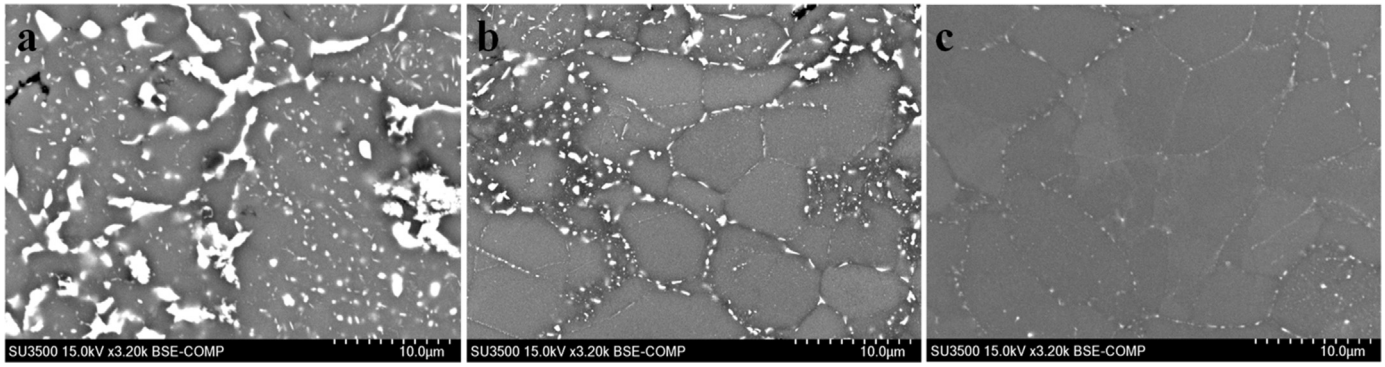

Fig. 4. BSE micrographs (high magnification) recorded from a T1 sample illustrating the typical microstructures observed within (a) region 1, (b) region 2 and (c) region 3 denoted in Fig. 3.

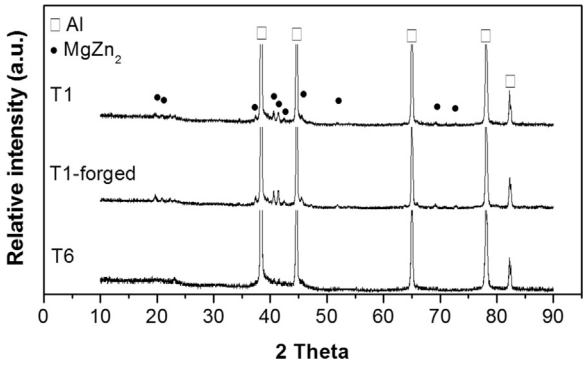

Fig. 5. XRD spectra acquired from T1, T1-forged and T6 samples.

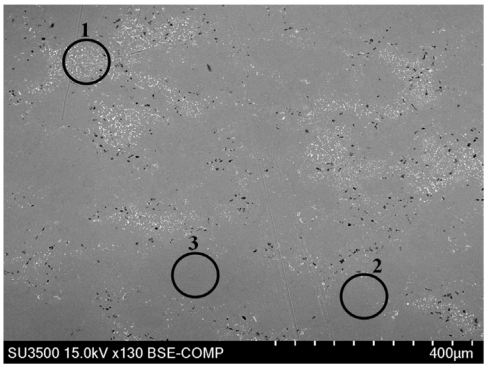

Fig. 6. Representative low magnification BSE micrograph recorded from a T6 sample.

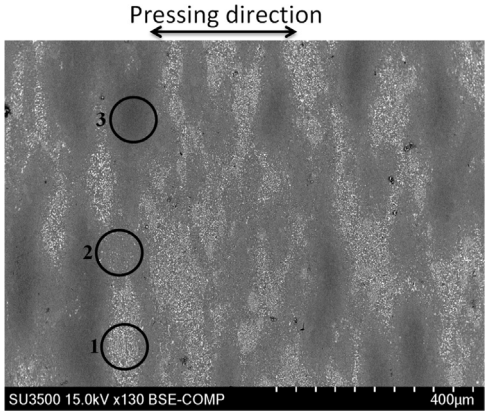

Fig. 8. Representative low magnification BSE micrograph recorded from a T1-forged sample.

Wert [37] that dynamic recrystallization (DRX) grains should contain substructure distinguishing them from SRX. Most of the equiaxed grains exhibited in Fig. 10b are identified by the lack of substructure, which implies that SRX was in fact operative. Besides that, a few equiaxed grains including substructure are also observed, which might be formed by DRX.

T6 heat treatment was also applied on the T1-forged sample and the density of the T6-forged sample measured by Archimedes was 99.0 ± 0.1% TD, while the image analysis technique showed a density of 99.2 ± 0.1%. The BSE micrograph of T6-forged sample is given in Fig. 11. Additional dissolution of the second phases originally present in the T1-forged sample occurred after the heat treatment, but there were still some sections wherein the secondary phases were obviously present (i.e. region 1 of Fig. 11).

High magnification BSE micrographs taken from the three regions

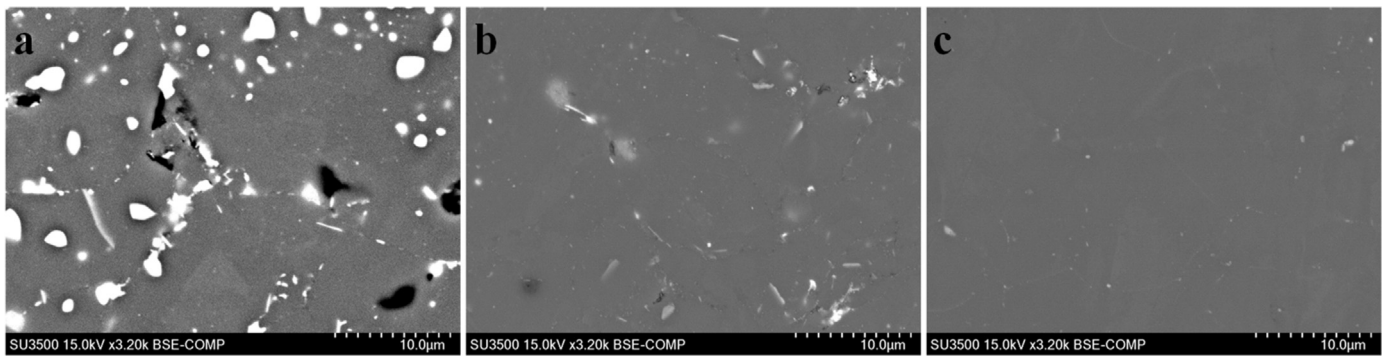

Fig. 7. BSE micrographs (high magnification) recorded from a T6 sample illustrating the typical microstructures observed within (a) region 1, (b) region 2 and (c) region 3 denoted in Fig. 6.

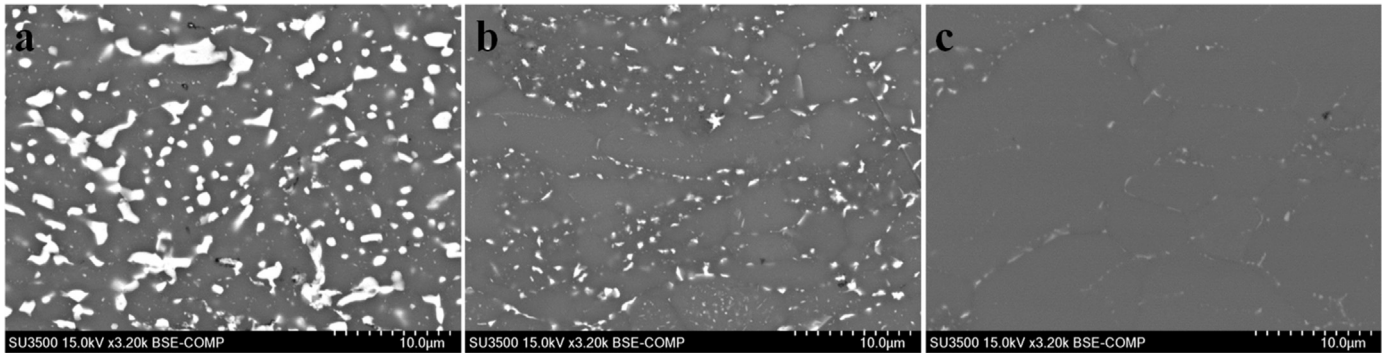

Fig. 9. BSE micrographs (high magnification) recorded from a T1-forged sample illustrating the typical microstructures observed within (a) region 1, (b) region 2 and (c) region 3 denoted in Fig. 8.

annotated in Fig. 11 are shown in Fig. 12. Here, a largely homogenized microstructure was observed within regions 2 and 3, whereas the second phases were not dissolved as effectively in region 1. EDS maps acquired from homogenized (regions 2 and 3) and partly homogenized (region 1) sections of the T6-forged sample are given in Figs. 13 and 14, respectively. It can be seen in Fig. 13 that the Zn map indicated an absence of areas locally enriched in this element thereby confirming that coarsened $MgZn_2$ precipitates had been dissolved. The precipitates that stemmed from the alloying elements in the master alloy (Fig. 14) contained Zn, Mg, and Cu, suggesting that these might be $MgZn_2$ with dissolved Cu [19,40,41]. Furthermore, the presence of O and Mg might be related to the formation of $MgAl_2O_4$ or MgO as a result of the reaction between Mg and the Al_2O_3 layer encasing the powder particles [42]. A similar observation has been reported by Rudianto et al. [43] for the sintering of Alumix 431D. Additionally, Toh et al. [44] demonstrated that the oxide layer of AA7475 alloy contains a possible mixture of magnesium and aluminum oxide. Also, as reported by Rudianto et al. [43] and Rudinsky et al. [19] clusters of Sn can be recognized in the microstructure.

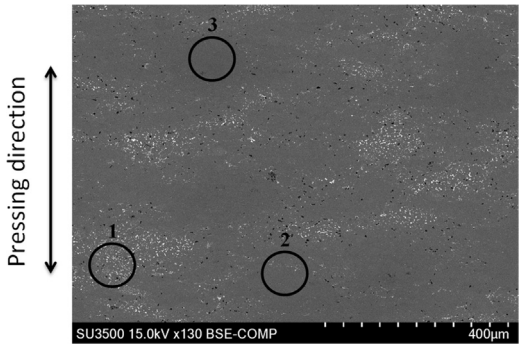

Fig. 11. Representative low magnification BSE micrograph recorded from a T6-forged sample.

3.3. Mechanical properties

Microhardness testing was performed on T1, T1-forged, T6, and T6-forged SPS samples with an emphasis on data acquisition within regions 1 and 3. The microhardness results for those regions and the average values are given in Table 3. It can be seen that there is a decrease in the hardness of T1-forged sample for the region 1 in comparison with T1 sample. This decrease in hardness after forging is most likely due to the growth of the precipitates as depicted in Figs. 4a and 9a. In terms of the T6 heat treated samples, hardness of the homogenized sections were comparable to reported values; Chua et al. [45] reported a hardness value of 87 HRB (180 HV) for SPS sintered AA7075 after T6 treatment, and it was equal to that of wrought AA7075-T6. The hardness measurement obtained after T6 treatment by LaDelpha et al. [26] for Alumix 431D processed by liquid phase sintering was 86 HRB (176 HV). On the other hand, the partly homogenized sections (region 1) of T6 samples exhibited a slight decrease in the hardness compared to region 3. However, this hardness was much more than the region 1 of T1 and T1-forged samples, indicating that some of the alloying elements have properly dissolved and the desired η' precipitates most likely nucleated

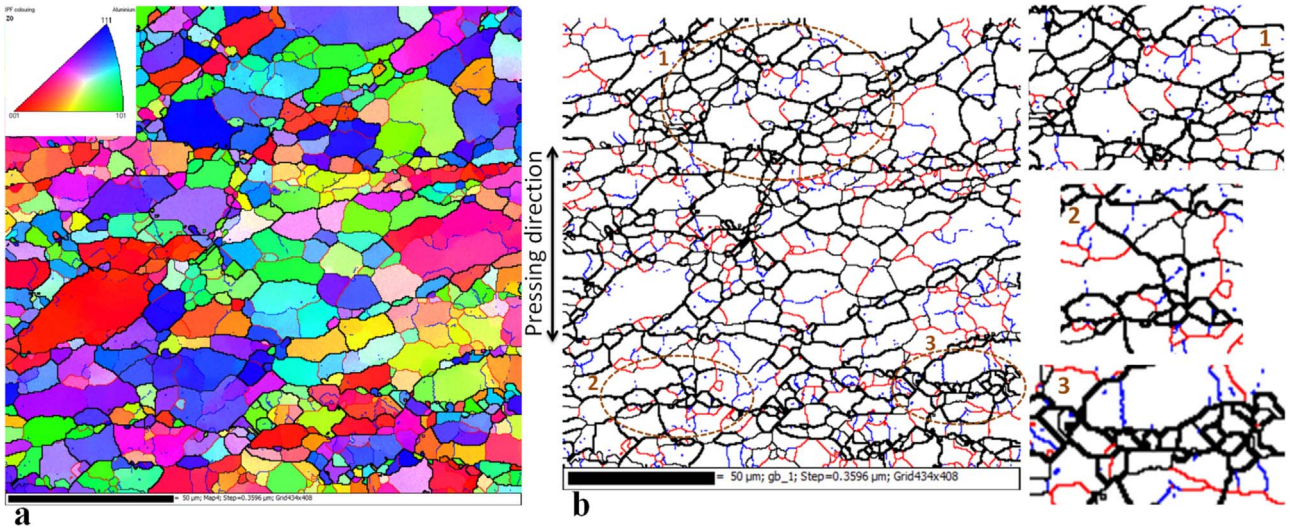

Fig. 10. EBSD analysis of a T1-forged sample (a) EBSD micrograph, (b).orientation imaging microscopy (OIM).

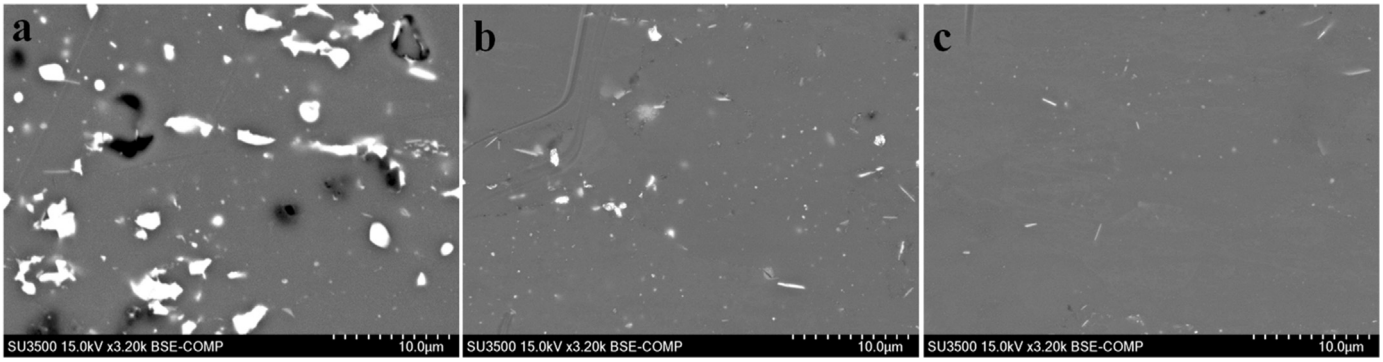

Fig. 12. BSE micrographs (high magnification) recorded from a T6-forged sample illustrating the typical microstructures observed within (a) region 1, (b) region 2 and (c) region 3 denoted in Fig. 11.

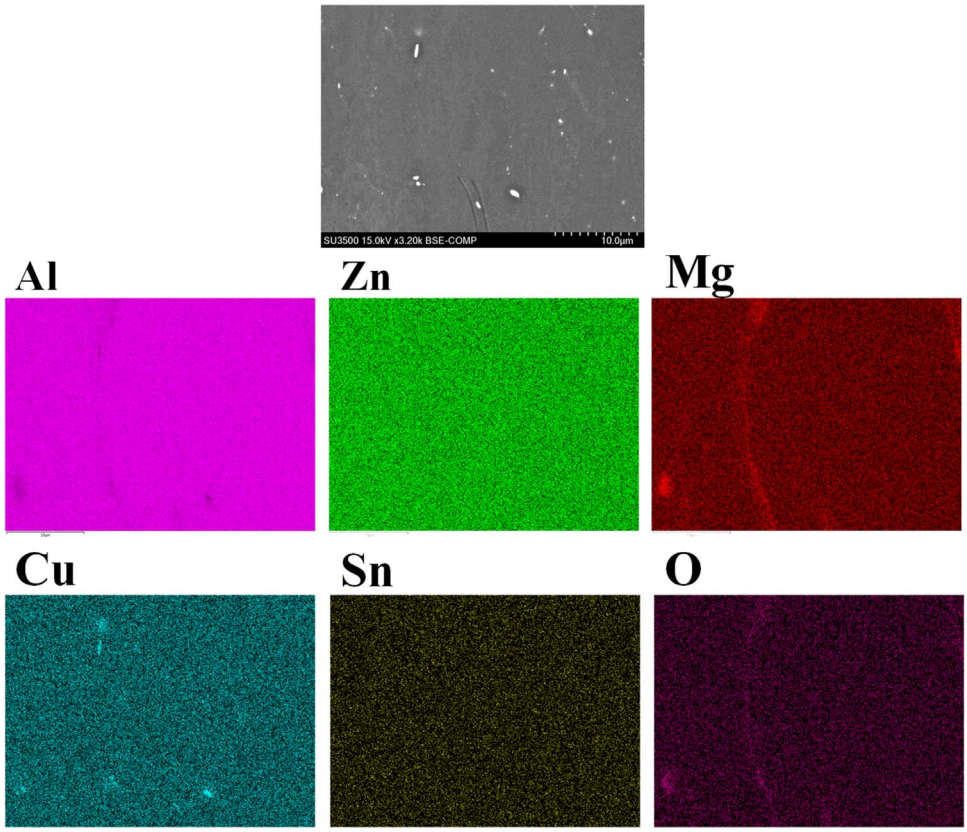

Fig. 13. EDS maps acquired from a homogenized section of a T6-forged sample.

during the aging period.

The flexural properties of the samples were evaluated by means of three-point bending. The resultant data are provided in Fig. 15. Flexural strength and strain values were improved after the forging process by 22% and 142%, respectively. The highest strength was obtained for the T6-forged sample, whereas its ductility was lowered similarly to that of the T6 sample. The improvement in the both flexural strength and strain after the forging process can be expected considering that the final density was further improved (more than 99% TD), as residual porosity is commonly known to have a detrimental effect on the mechanical properties of P/M products [46]. Furthermore, the oxide network present in the sintered product had likely been disrupted through hot working stage of processing and this too is known to improve the mechanical performance of sintered aluminum P/M alloys [47].

SEM images acquired normal and transverse to the fracture surfaces developed in T1 and T1-forged samples are shown in Fig. 16. Counterpart images for T6 and T6-forged materials are shown in Fig. 17. The fracture surface of the T1 sample (Fig. 16a) elucidate prior particle boundaries, indicating a sign of incomplete bonding between the starting powder particles. Additionally, the transverse view of this sample, presented in Fig. 16b, indicated that fracture had progressed along prior particle boundaries. The mechanical properties of the sintered samples can be deteriorated by the presence of prior particle boundaries, which comes from the incomplete bonding of the powder particles due to the native surface oxide layer [48,49]. It was previously shown that SPS of pure Al provided good particle bonding where the oxide layer was mostly disrupted [17]. In the case of Alumix 431D, which is equivalent to AA7075, the oxide layer is different than the one present on pure Al. It has a composite type of oxide layer coming from magnesium oxide and aluminum oxide [20]. Therefore, the pressure during the initial sintering of Al alloy might not have been enough to disrupt the oxide layer unlike that present on soft, pure Al [17,20]. The application of forming processes to sintered Al products, such as forging, can disrupt the oxide film and enhance the metallurgical bonding [1]. As an indication of the improvement in the metallurgical bonding, the fracture surface of the T1-forged sample, shown in Fig. 16c, has

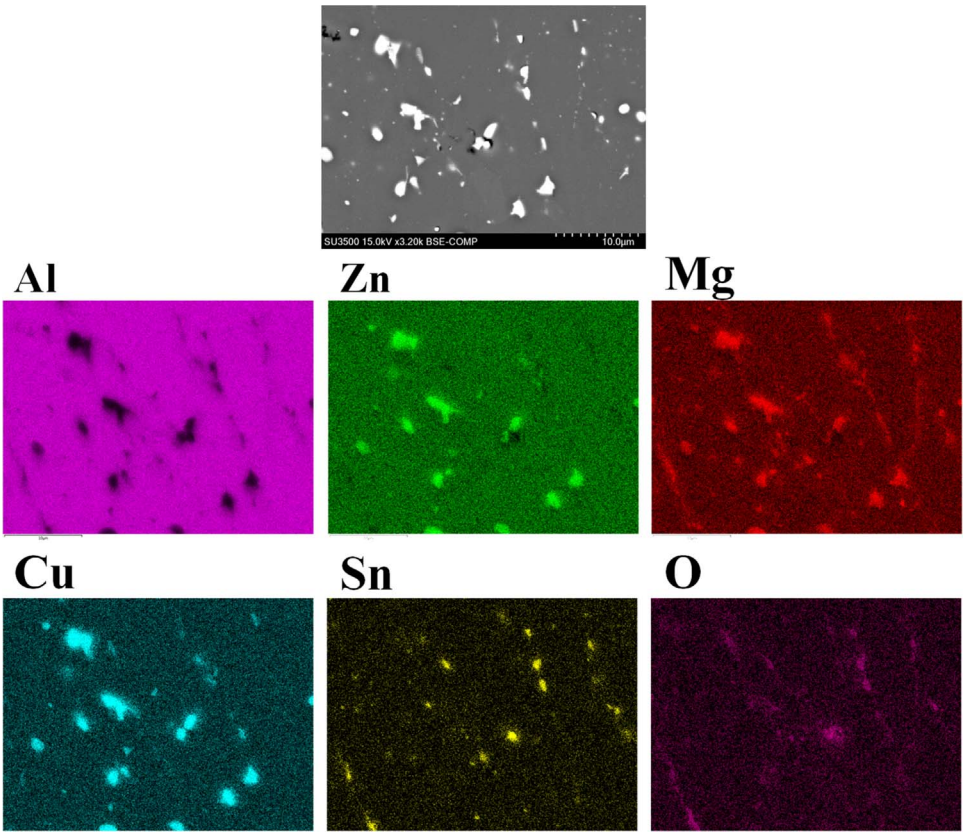

Fig. 14. EDS maps of acquired from a partly homogenized section of a T6-forged sample.

Table 3
Microhardnesses of T1, T1-forged, T6, and T6-forged samples.

	Region 1	Region 3	Average
T1 (HV)	118 ± 1	79 ± 8	99 ± 10
T1-forged (HV)	105 ± 2	79 ± 7	92 ± 7
T6 (HV)	159 ± 5	173 ± 3	166 ± 4
T6-forged (HV)	160 ± 9	172 ± 3	166 ± 5

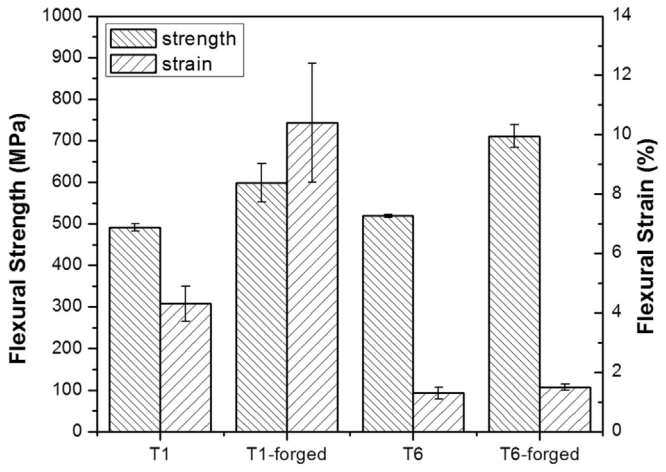

Fig. 15. Flexural properties measured for the T1, T1-forged, T6 and T6-forged samples.

more pronounced dimples showing the transgranular ductile fracture via microvoid formation, growth, and coalescence [50] and the presence of prior particle boundaries was now reduced. It can also be seen from the transverse view (Fig. 16d) that transgranular fracture was now more prevalent in comparison with Fig. 16b. It is also notable that the occurrence of recrystallization can make an additional contribution towards the improvement of the flexural properties after the forging process. In this sense, it has been reported that [51] the room temperature mechanical properties of AA7075 plates were improved after hot rolling at 450 °C and that the gains were attributed to recrystallization.

It can be seen from Fig. 15 that the flexural strain of the T1 sample decreased after processing into the T6 temper. Although the age hardening heat treatment is expected to lower the ductility while increasing the strength [52], the significant loss in the ductility of this study is believed to occur due to the lack of cohesion between particles that can be intensified during the quenching step. Similar observations were also seen in another study [19]. The prior particle boundaries observed in Fig. 17a and in Fig. 17b indicate that fracture again occurred between the particles. Since the strength and the strain of T1 samples was improved after forging process, it can be expected that the same trend will be maintained after T6 treatment. Even though this was the case for the strength, the ductility of the T6-forged sample was equivalent to T6 sample, thereby failing to follow the expected trend. Therefore, the loss in the ductility might not only be the lack of the cohesion between particles. During the diffusion of a phase into a matrix, the dissolved phase can leave a hole in the matrix [53]. The arrows in Fig. 17 indicate the formation of the voids and the size of these holes was in the range of 1–4 μm. Similarly, the holes within the same range have been seen in the region 1 of T6 and T6-forged samples (Figs. 7a and 12a). The ductility of the powder metallurgy product is decreased by residual porosity in an exponential manner [54]. Therefore, these voids were observed after heat treatment, which might arise from the dissolution of $MgZn_2$ into the Al matrix, leading to the reduction of ductility in addition to the effect of T6 temper.

4. Conclusions

In this study, Alumix 431D powder was sintered and forged through

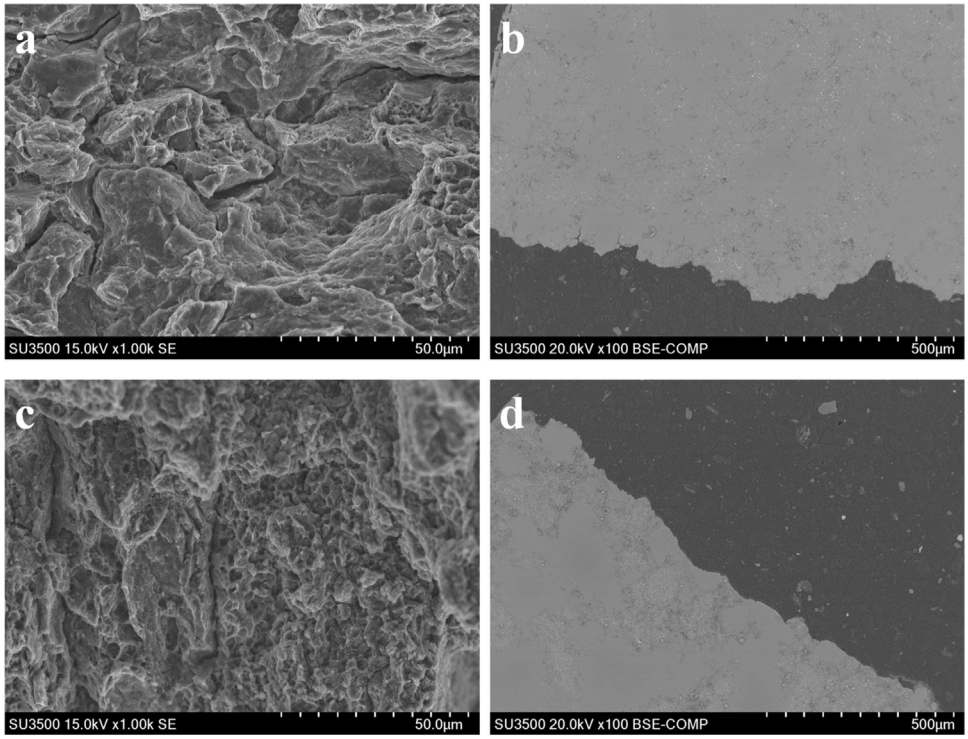

Fig. 16. SEM images of the bending-induced fracture observed in T1 ((a) normal and (b) transverse) and T1-forged ((c) normal and (d) transverse) samples.

spark plasma sintering and T6 heat treatment was applied to both samples. Near fully dense samples (99.1 ± 0.3% TD) were obtained after the sintering and it was 99.8 ± 0.1% TD after forging. Microstructure and mechanical properties were investigated before and after heat treatment. Flexural strength and strain were improved after the forging process. This improvement was attributed to the enhancement of the metallurgical bonding in addition to the slight increase in the density and occurrence of recrystallization. A microhardness that was comparable to that of wrought counterpart was obtained after the T6 temper. The significant loss in the ductility after the heat treatment was mainly ascribed to the formation of the voids due the dissolution of $MgZn_2$, and lack of cohesion between particles.

Acknowledgement

The authors would like to acknowledge AUTO 21 (Grant no. C502-CPM) for their financial support and the Aluminum Research Centre – REGAL. The authors would like to thank The Council of Higher

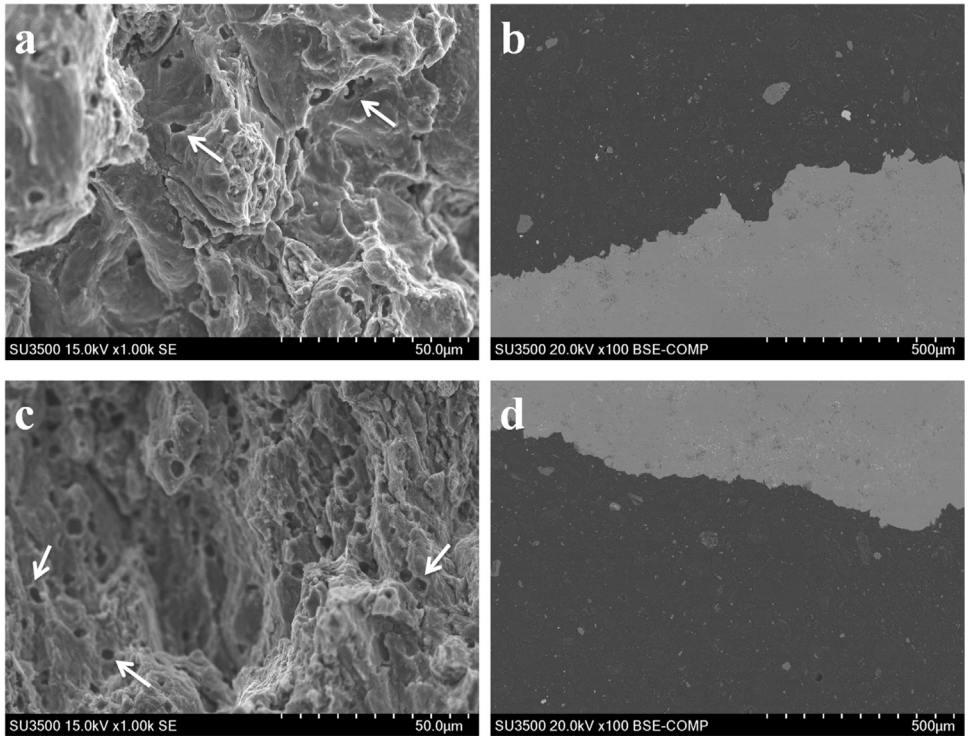

Fig. 17. SEM images of the bending-induced fracture observed in T6 ((a) normal and (b) transverse) and T6-forged ((c) normal and (d) transverse) samples.

Education of Turkey and Marmara University for scholarships to Mr. Tünçay. The authors also thank to Mr. Abhi Ghosh for his assistance with EBSD analysis.

References

[1] T.C. Joshi, U. Prakash, V.V. Dabhade, Microstructural development during hot forging of Al 7075 powder, J. Alloy. Compd. 639 (2015) 123–130, http://dx.doi.org/10.1016/j.jallcom.2015.03.099.

[2] M.A. Jabbari Taleghani, E.M. Ruiz Navas, J.M. Torralba, Microstructural and mechanical characterisation of 7075 aluminium alloy consolidated from a premixed powder by cold compaction and hot extrusion, Mater. Des. 55 (2014) 674–682, http://dx.doi.org/10.1016/j.matdes.2013.10.028.

[3] G.B. Schaffer, Powder processed aluminium alloys, Mater. Forum 28 (2004) 65–74.

[4] ECKA Granules On-Line Product Brochure Alumix-431D, 2017. ⟨https://www.ecka-granules.com/en/products/aluminum-and-aluminum-alloys/⟩.

[5] M. Omori, Sintering, consolidation, reaction and crystal growth by the spark plasma system (SPS), Mater. Sci. Eng.: A 287 (2000) 183–188, http://dx.doi.org/10.1016/S0921-5093(00)00773-5.

[6] M.S. Mohammadi, A. Simchi, C. Gierl, Phase formation and microstructural evolution during sintering of Al-Zn-Mg-Cu alloys, Powder Metall. 53 (2010) 62–70, http://dx.doi.org/10.1179/003258908×344707.

[7] Z.A. Munir, D.V. Quach, M. Ohyanagi, Electric current activation of sintering: a review of the pulsed electric current sintering process, J. Am. Ceram. Soc. 94 (2011) 1–19, http://dx.doi.org/10.1111/j.1551-2916.2010.04210.x.

[8] Z.A. Munir, U. Anselmi-Tamburini, M. Ohyanagi, The effect of electric field and pressure on the synthesis and consolidation of materials: a review of the spark plasma sintering method, J. Mater. Sci. 41 (2006) 763–777, http://dx.doi.org/10.1007/s10853-006-6555-2.

[9] O. Guillon, J. Gonzalez-Julian, B. Dargatz, T. Kessel, G. Schierning, J. Räthel, M. Herrmann, Field-assisted sintering technology/spark plasma sintering: mechanisms, materials, and technology developments, Adv. Eng. Mater. 16 (2014) 830–849, http://dx.doi.org/10.1002/adem.201300409.

[10] G. Xie, O. Ohashi, T. Yoshioka, M. Song, K. Mitsuishi, H. Yasuda, K. Furuya, T. Noda, Effect of interface behavior between particles on properties of pure Al powder compacts by spark plasma sintering, Mater. Trans. 42 (2001) 1846–1849, http://dx.doi.org/10.2320/matertrans.42.1846.

[11] T. Nagae, M. Yokota, M. Nose, S. Tomida, T. Kamiya, S. Saji, Effects of pulse current on an aluminum powder oxide layer during pulse current pressure sintering, Mater. Trans. 43 (2002) 1390–1397, http://dx.doi.org/10.2320/matertrans.43.1390.

[12] G. Xie, O. Ohashi, K. Chiba, N. Yamaguchi, M. Song, K. Furuya, T. Noda, Frequency effect on pulse electric current sintering process of pure aluminum powder, Mater. Sci. Eng.: A 359 (2003) 384–390, http://dx.doi.org/10.1016/S0921-5093(03)00393-9.

[13] G. Xie, O. Ohashi, M. Song, K. Furuya, T. Noda, Behavior of oxide film at the interface between particles in sintered Al powders by pulse electric-current sintering, Metall. Mater. Trans. A 34 (2003) 699–703, http://dx.doi.org/10.1007/s11661-003-0104-2.

[14] M. Zadra, F. Casari, L. Girardini, A. Molinari, Spark plasma sintering of pure aluminium powder: mechanical properties and fracture analysis, Powder Metall. 50 (2007) 40–45, http://dx.doi.org/10.1179/174329007×186417.

[15] H. Kwon, D. Park, Y. Park, J. Silvain, A. Kawasaki, Y. Park, Spark plasma sintering behavior of pure aluminum depending on various sintering temperatures, Met. Mater. Int. 16 (2010) 71–75, http://dx.doi.org/10.1007/s12540-010-0071-2.

[16] G.A. Sweet, M. Brochu, R.L. Hexemer Jr, I.W. Donaldson, D.P. Bishop, Microstructure and mechanical properties of air atomized aluminum powder consolidated via spark plasma sintering, Mater. Sci. Eng.: A 608 (2014) 273–282, http://dx.doi.org/10.1016/j.msea.2014.04.078.

[17] M.M. Tünçay, L. Nguyen, P. Hendrickx, M. Brochu, Evaluation of the particle bonding for aluminum sample produced by spark plasma sintering, J. Mater. Eng. Perform. 25 (2016) 4521–4528, http://dx.doi.org/10.1007/s11665-016-2275-1.

[18] D. Garbiec, P. Siwak, Study on microstructure and mechanical properties of spark plasma sintered Alumix 431 powder, Powder Metall. 59 (2016) 242–248, http://dx.doi.org/10.1080/00325899.2016.1169362.

[19] S. Rudinsky, P. Hendrickx, D.P. Bishop, M. Brochu, Spark plasma sintering and age hardening of an Al–Zn–Mg alloy powder blend, Mater. Sci. Eng.: A 650 (2016) 129–138, http://dx.doi.org/10.1016/j.msea.2015.10.029.

[20] P. Hendrickx, M.M. Tünçay, M. Brochu, Recyclability assessment of Al 7075 chips produced by cold comminution and consolidation using spark plasma sintering, Can. Metall. Q. 55 (2016) 94–103, http://dx.doi.org/10.1080/00084433.2015.1125094.

[21] K. Lange, Handbook of Metal Forming, McGraw-Hill, New York, 1985.

[22] G.E. Dieter, H.A. Kuhn, S.L. Semiatin, Handbook of Workability and Process Design, ASM International, Materials Park, OH, 2003.

[23] ASTM B963-13, Standard Test Methods for Oil Content, Oil-Impregnation Efficiency, and Interconnected Porosity of Sintered Powder Metallurgy (PM) Products Using Archimedes' Principle, ASTM International, West Conshohocken, PA, 2013.

[24] J.M. Martín, T. Gómez-Acebo, F. Castro, Sintering behaviour and mechanical properties of PM Al-Zn-Mg-Cu alloy containing elemental Mg additions, Powder Metall. 45 (2002) 173–180, http://dx.doi.org/10.1179/003258902225002460.

[25] J. Milligan, M. Brochu, Cladding AA7075 with a cryomilled Al–12Si alloy using spark plasma sintering, Mater. Sci. Eng.: A 578 (2013) 323–330, http://dx.doi.org/10.1016/j.msea.2013.04.113.

[26] A.D.P. LaDelpha, H. Neubing, D.P. Bishop, Metallurgical assessment of an emerging Al–Zn–Mg–Cu P/M alloy, Mater. Sci. Eng.: A 520 (2009) 105–113, http://dx.doi.org/10.1016/j.msea.2009.05.039.

[27] T. Pieczonka, J. Kazior, A. Szewczyk-Nykiel, M. Hebda, M. Nykiel, Effect of atmosphere on sintering of Alumix 431D powder, Powder Metall. 55 (2012) 354–360, http://dx.doi.org/10.1179/1743290112Y.0000000015.

[28] X. Fan, D. Jiang, Q. Meng, L. Zhong, The microstructural evolution of an Al–Zn–Mg–Cu alloy during homogenization, Mater. Lett. 60 (2006) 1475–1479, http://dx.doi.org/10.1016/j.matlet.2005.11.049.

[29] R.E. Smallman, A.H.W. Ngan, Physical Metallurgy and Advanced Materials, 7th edition, Elsevier, Oxford, UK, 2007.

[30] Y. Lang, Y. Cai, H. Cui, J. Zhang, Effect of strain-induced precipitation on the low angle grain boundary in AA7050 aluminum alloy, Mater. Des. 32 (2011) 4241–4246, http://dx.doi.org/10.1016/j.matdes.2011.04.025.

[31] A. Deschamps, G. Fribourg, Y. Bréchet, J.L. Chemin, C.R. Hutchinson, In situ evaluation of dynamic precipitation during plastic straining of an Al–Zn–Mg–Cu alloy, Acta Mater. 60 (2012) 1905–1916, http://dx.doi.org/10.1016/j.actamat.2012.01.002.

[32] W.T. Huo, J.T. Shi, L.G. Hou, J.S. Zhang, An improved thermo-mechanical treatment of high-strength Al–Zn–Mg–Cu alloy for effective grain refinement and ductility modification, J. Mater. Process. Technol. 239 (2017) 303–314, http://dx.doi.org/10.1016/j.jmatprotec.2016.08.027.

[33] L.M. Yan, J. Shen, J.P. Li, Z.B. Li, Z.L. Tang, Dynamic recrystallization of 7055 aluminum alloy during hot deformation, Mater. Sci. Forum 650 (2010) 295–301, http://dx.doi.org/10.4028/www.scientific.net/MSF.650.295.

[34] T. Sakai, J.J. Jonas, Overview no. 35 Dynamic recrystallization: mechanical and microstructural considerations, Acta Metall. 32 (1984) 189–209, http://dx.doi.org/10.1016/0001-6160(84)90049-X.

[35] C. Shi, J. Lai, X.-G. Chen, Microstructural evolution and dynamic softening mechanisms of Al-Zn-Mg-Cu alloy during hot compressive deformation, Materials 7 (2014) 244 ⟨http://www.mdpi.com/1996-1944/7/1/244⟩.

[36] R.E. Rupp, A.J. Weldon, T.J. Watt, R. Perez-Bustamante, K. Takata, E.M. Taleff, Recrystallization in Al-Mg Alloys after Hot Compression, Light Metals 2016 John Wiley & Sons, Inc, Hoboken, NJ, USA, 2016, pp. 163–167.

[37] M.A. Zaidi, J.A. Wert, 5 – Thermomechanical processing of aluminum alloys, in: V. A.K, D. R.D (Eds.), Treatise on Materials Science and Technology, Elsevier, San Diego, CA, USA, 1989, pp. 137–170.

[38] H.J. McQueen, Hot Deformation and Processing of Aluminum Alloys, CRC Press, Boca Raton, 2011.

[39] H.J. McQueen, Examining the mechanisms of dynamic recrystallization (DRX) in two-phase Al alloys, in: ICAA13: 13th International Conference on Aluminum Alloys, John Wiley & Sons, Inc., 2012, pp. 1761–1766.

[40] M.J. Styles, T.J. Bastow, M.A. Gibson, C.R. Hutchinson, Substitution of Cu and/or Al in η phase (MgZn2) and the implications for precipitation in Al–Zn–Mg–(Cu) alloys, Intermetallics 49 (2014) 40–51, http://dx.doi.org/10.1016/j.intermet.2014.01.012.

[41] J.-T. Liu, Y.-A. Zhang, X.-W. Li, Z.-H. Li, B.-Q. Xiong, J.-S. Zhang, Phases and microstructures of high Zn-containing Al–Zn–Mg–Cu alloys, Rare Met. 35 (2016) 380–384, http://dx.doi.org/10.1007/s12598-014-0222-6.

[42] G. Xie, O. Ohashi, M. Song, K. Mitsuishi, K. Furuya, Reduction mechanism of surface oxide films and characterization of formations on pulse electric-current sintered Al–Mg alloy powders, Appl. Surf. Sci. 241 (2005) 102–106, http://dx.doi.org/10.1016/j.apsusc.2004.09.025.

[43] H. Rudianto, G.J. Jang, S.S. Yang, Y.J. Kim, I. Dlouhy, Evaluation of sintering behavior of premix Al-Zn-Mg-Cu alloy powder, Adv. Mater. Sci. Eng. 2015 (2015) 8, http://dx.doi.org/10.1155/2015/987687.

[44] S.K. Toh, D.G. McCulloch, J. Du Plessis, P.J.K. Paterson, A.E. Hughes, D. Jamieson, B. Rout, J.M. Long, A. Stonham, An investigation of the native oxide of aluminum alloy 7475-T7651 using XPS, AES, TEM, EELS, GDOES and RBS, Surf. Rev. Lett. 10 (2003) 365–371, http://dx.doi.org/10.1142/s0218625×0300530x.

[45] A.S. Chua, M. Brochu, D.P. Bishop, Spark plasma sintering of prealloyed aluminium powders, Powder Metall. 58 (2015) 51–60, http://dx.doi.org/10.1179/1743290114Y.0000000105.

[46] M.A. Meyers, A. Mishra, D.J. Benson, Mechanical properties of nanocrystalline materials, Prog. Mater. Sci. 51 (2006) 427–556, http://dx.doi.org/10.1016/j.pmatsci.2005.08.003.

[47] I.A. MacAskill, A.D.P. LaDepha, J.H. Milligan, J.J. Fulton, D.P. Bishop, Effects of cold and hot densification on the mechanical properties of a 7XXX series powder metallurgy alloy, Powder Metall. 52 (2009) 304–310, http://dx.doi.org/10.1179/174329009×409723.

[48] S.C. Yoon, S.I. Hong, S.H. Hong, H.S. Kim, Densification and conolidation of powders by equal channel angular pressing, Mater. Sci. Forum 534–536 (2007) 253–256.

[49] M. Brochu, T. Zimmerly, L. Ajdelsztajn, E.J. Lavernia, G. Kim, Dynamic consolidation of nanostructured Al–7.5%Mg alloy powders, Mater. Sci. Eng.: A 466 (2007) 84–89, http://dx.doi.org/10.1016/j.msea.2007.02.028.

[50] H.S.Y.S.Q. Wang, Z.Y. Zhang, G.H. Min, H. Yu, Microstructural evolution and mechanical properties of powder hot extruded Al-Zn-Mg-Cu alloy, Adv. Mater. Res. 79–82 (2009) 2015–2018.

[51] A. Abolhasani, A. Zarei-Hanzaki, H.R. Abedi, M.R. Rokni, The room temperature mechanical properties of hot rolled 7075 aluminum alloy, Mater. Des. 34 (2012) 631–636, http://dx.doi.org/10.1016/j.matdes.2011.05.019.

[52] A.D. Isadare, B. Aremo, M.O. Adeoye, O.J. Olawale, M.D. Shittu, Effect of heat treatment on some mechanical properties of 7075 aluminium alloy, Mater. Res.-Ibero-Am. J. Mater. 16 (2013) 190–194, http://dx.doi.org/10.1590/s1516-14392012005000167.

[53] M. Brochu, B. Gauntt, T. Zimmerly, A. Ayala, R. Loehman, Fabrication of UHTCs by conversion of dynamically consolidated Zr + B and Hf + B powder mixtures, J. Am. Ceram. Soc. 91 (2008) 2815–2822, http://dx.doi.org/10.1111/j.1551-2916.2008.02550.x.

[54] R.M. German, Powder Metallurgy and Particulate Materials Processing, MPIF, Princeton, 2005.